

Nanoplastic Analysis with Nanoelectromechanical System Fourier Transform Infrared Spectroscopy: NEMS–FTIR

Jelena Timarac–Popović^{1,2*}, Johannes Hiesberger^{1,2}, Eldira Šesto¹, Niklas Luhmann²,
Ariane Giesriegl¹, Hajrudin Bešić¹, Josiane P. Lafleur², and Silvan Schmid^{1*}

¹*TU Wien, Institute of Sensor and Actuator Systems, Gusshausstrasse 27–29, 1040 Vienna, Austria.*

²*Invisible–Light Labs GmbH, Taubstummengasse 11, 1040 Vienna, Austria.*

(Dated: April 18, 2025)

This paper presents a photothermal infrared (IR) spectroscopy technique based on a nanoelectromechanical system, which is coupled to a commercial Fourier transform infrared spectrometer (NEMS–FTIR) as a promising solution for the chemical characterization and quantification of nanoplastics. Polystyrene (PS), polypropylene (PP), and polyvinyl chloride (PVC) nanoparticles with nominal diameters of 100, 54, and 262 nm, respectively, were analyzed by NEMS–FTIR with limits of detection (LoD) of 353 pg for PS, 102 pg for PP, and 355 pg for PVC. The PS mass deposited on the NEMS chips was estimated from the measured absorbance values and the attenuation coefficient of PS. The wide spectral range of the FTIR allowed the identification of individual polymer nanoparticles from a mixture. The potential of NEMS–FTIR for the analysis of real–world samples was evaluated by confirming the presence of polyamide (PA) particles released from commercial tea bags during brewing. Accelerated aging of the tea bags under elevated temperature and UV radiation showed continuous release of PA particles over time.

Keywords: nanoplastics, nanoparticles, NEMS–FTIR, Fourier transform infrared spectroscopy, photothermal sensing, nanoelectromechanical system, nanomechanical resonator, tea bag.

INTRODUCTION

Nanoplastics have become ubiquitous, posing significant challenges linked to their high reactivity, potential to transport pollutants, and widespread dispersion across ecosystems [1–7]. Their ability to penetrate deep into tissues underscores the need for precise chemical characterization and monitoring [8].

Sampling of nanoplastic particles is particularly challenging due to their nanoscale dimensions and low concentrations, which often exceed the capabilities of many analytical techniques to effectively characterize these tiny fragments [9–11]. While well–established techniques exist nowadays for microplastic detection and identification, identifying nanoplastics is more challenging.

Surface–enhanced Raman spectroscopy (SERS) has emerged as a promising technique. Zhou et al. [12] and Hu et al. [13] successfully achieved LoDs as low as 5 $\mu\text{g/mL}$ for PS particles as small as 50 nm. Optical–photothermal IR (O–PTIR)

spectroscopy has also proven very effective for the imaging of individual PS nanoparticles as small as 250 nm in mammalian tissues [14] and identification of plastics (> 600 nm) containing polysiloxanes and imides, originating from the steam disinfection of silicone baby teats [15].

Mass spectrometry–based techniques can be used to chemically identify particles smaller than 1 μm and are often synergistically combined with other methods to reliably detect, quantify, and identify nanoplastics [10, 11, 16]. Pyrolysis–gas chromatography–mass spectrometry (Py–GC/MS) has been extensively applied to detect various types of nanoplastics, including PS, PP, polycarbonate (PC), polyethylene terephthalate (PET), polymethyl methacrylate (PMMA), PVC, polyethylene (PE), and Nylon 6/66, with reported LoDs as low as 1 ng/L [17, 18]. Using the same technique, Li et al. [19] estimated a LoD of 10 ng for two polymer types of nanoplastics in water, PS, and PMMA. A combination of atomic force

microscope-IR (AFM-IR) spectroscopy and Py-GC/MS was also used to detect and quantify PE and PVC particles (20–1000 nm), with LoDs of 0.28 μg for PE and 1.54 μg for PVC [20]. Alternative approaches, such as thermal desorption-proton transfer reaction-mass spectrometry (TD-PTR-MS), demonstrated remarkable sensitivity, with Materić et al. [21] detecting pure 1 μm PS particles with an LoD of 0.34 ng, allowing detection of these particles in environmental samples as small as 1 mL without preconcentration.

Many studies have analyzed the release of micro- and nanoplastic particles from tea bags during tea preparation using different analytical methods such as scanning transmission X-ray microscopy (STXM) in combination with near-edge X-ray absorption fine-structure spectroscopy (NEXAFS) [22], IR photothermal heterodyne imaging (IR-PHI) [23], Raman spectroscopy [24], and attenuated total reflectance-FTIR (ATR-FTIR) [25, 26]. These, however, often require sample preconcentration steps or sample preparation procedures which differ from a standard tea brewing procedure.

Although existing analytical techniques offer high sensitivity and specificity, they remain impractical for routine environmental monitoring, particularly for water suppliers and official control laboratories [27]. Mass spectrometry-based techniques provide excellent precision, but their complexity and cost hinder their use in routine environmental monitoring [11, 16, 28]. SERS suffers from issues such as spectral artifacts and reliance on carefully engineered substrates, limiting its versatility [11]. With its broad spectral range, AFM-IR faces challenges with low signal-to-noise ratio (SNR) and slow imaging speed [29]. O-PTIR also encounters limitations due to its narrow spectral range and slow imaging speed, further compounded by the very high acquisition cost [29].

Nanoelectromechanical IR spectroscopy (NEMS-IR) is a technique based on the photothermal effect that has been introduced in recent years. It employs NEMS membrane resonators, or chips, as its key component [30, 31]. The NEMS chip can be used simultaneously as a sample carrier and detector. The NEMS chips,

typically consisting of a pre-stressed silicon nitride (SiN) membrane, are robust and allow for a wide variety of sampling techniques [32], including direct aerosol collection [30, 31, 33] and drop casting. When a sample deposited on the NEMS chip's surface absorbs IR light, local heating occurs, causing thermal expansion and tensile stress reduction. The corresponding frequency detuning of the NEMS chip is proportional to the absorbed power, and the frequency shift can be monitored using a closed-loop oscillation scheme in combination with a frequency counter, as demonstrated by Bešić et al. [34, 35]. NEMS-IR has shown picogram sensitivity at room temperature over a large spectral range, from the ultraviolet to the far-IR [32]. This technique has been used to analyze polymer nanoparticles [36, 37], pharmaceutical compounds [31, 38], polymer micelles [39], thin polymer films [40] and explosives [41]. NEMS-IR with in-situ thermal desorption (TD) analysis has also been demonstrated for separating simple analyte mixtures by Luhmann et al. [30].

NEMS-IR has only been used for dispersive spectroscopy, typically relying on expensive, narrowband tunable quantum cascade lasers (QCLs). This paper presents NEMS-FTIR spectroscopy as a new approach to the chemical characterization and quantification of nanoplastics. While cantilevers have previously been used as photothermal detectors in conjunction with FTIR sources [42], the approach presented here centers on NEMS membrane resonators shown in Fig. 1A, offering enhanced sensitivity and sampling flexibility. NEMS-FTIR uses a commercially available FTIR spectrometer as a light source, as shown in Fig. 1B, instead of a QCL. NEMS-FTIR, therefore, offers a powerful new approach for the routine monitoring and characterization of nanoplastics by combining the exceptional sensitivity and versatility of nanomechanical photothermal sensing with the broad spectral coverage and user-friendly operation of commercially available FTIR spectrometers. Here we demonstrate the power and versatility of this technique for the sampling, detection, characterization, and quantification of nanoplastics in aqueous samples and

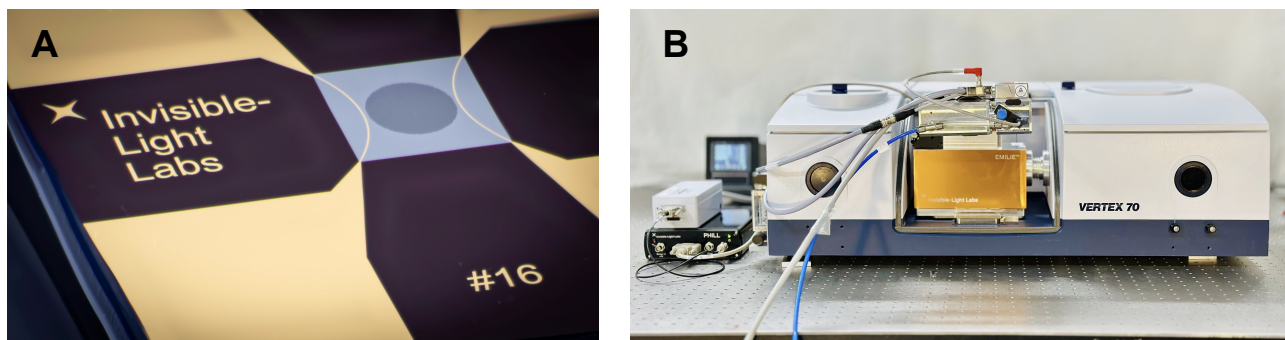


Fig. 1. Experimental setup for NEMS-FTIR analysis. (A) A NEMS sampling and sensing chip (Invisible-Light Labs GmbH, Austria). The central square NEMS membrane resonator is made of SiN and has a lateral size of $1 \times 1 \text{ mm}^2$ and a thickness of $\sim 50 \text{ nm}$. It features a circular micro perforation in its center. (B) An FTIR spectrometer (Vertex 70, Bruker Corporation, MA, USA) equipped with the nanoelectromechanical IR analyzer (EMILIE™, Invisible-Light Labs GmbH, Austria) for NEMS-FTIR analysis.

nylon tea bag leachates.

RESULTS

Single nanoplastic dispersions

Aqueous dispersions of three different polymers, PS (nominal diameter: 100 nm), PP (nominal diameter: 54 nm), and PVC (nominal diameter: 262 nm), were deposited via drop casting on individual NEMS chips. Fig. 2A–C shows PS, PP, and PVC nanoparticles after deposition onto the central circular perforation of the NEMS chips (see Fig. 1A). These scanning electron microscopy (SEM) images highlight the generally spherical morphology and relatively uniform size distributions of the nanoplastic particles studied. However, there are areas of nanoparticle agglomerations on the membrane of the NEMS chip caused by the coffee ring effect during droplet drying (see Fig. S1 in Supplementary Materials). After the nanodrop dispersion has dried, all nanoparticles are confined within the perforated area of the NEMS chip.

Spectral data was obtained by depositing a 20 nL nanodrop of various nanoplastic concentrations on the NEMS chips ($N=3$ for each concentration). The NEMS-FTIR spectra of PS nanoplastic particles for each concentration, power-corrected, normalized using the SiN peak at 835 cm^{-1} , and converted into absorbance, are shown in Fig. 2D. The details of the spectral processing procedure are described in the "Processing of NEMS-

FTIR spectra" in the Materials and Methods section. The spectra of PP and PVC nanoparticles are available in the Supplementary Materials in Figs. S2 and S3, respectively.

The IR peaks in the NEMS-FTIR spectra of PS nanoparticles correspond to data reported in the literature [43–46]. Notably, PS is characterized by a mono-substituted benzene ring, as evidenced by a series of weak overtone and combination bands between 2000 and 1650 cm^{-1} (so-called 'benzene fingers'), often difficult to detect in the spectrum if the concentration of molecules containing the benzene ring is low [45], and the peaks at 753 and 700 cm^{-1} . However, these peaks are clearly visible in the NEMS-FTIR spectra of PS, even for the very low masses in the nanogram range. The NEMS-FTIR spectra of PP and PVC nanoparticles also display peaks corresponding to their respective vibrational modes. The positions of these peaks are in accordance with prior studies using FTIR spectroscopy [45, 47], as well as with the measurements obtained using early IR spectrophotometers employing prisms [48]. NEMS-FTIR does not suffer from the red-shift typically associated with measurements performed by ATR-FTIR, as observed in previous studies [49]. In ATR-FTIR, slight shifts in some peak positions are observed due to differences in how this technique probes the sample, particularly the interaction of the evanescent wave with the sample surface and its dependence on refractive index

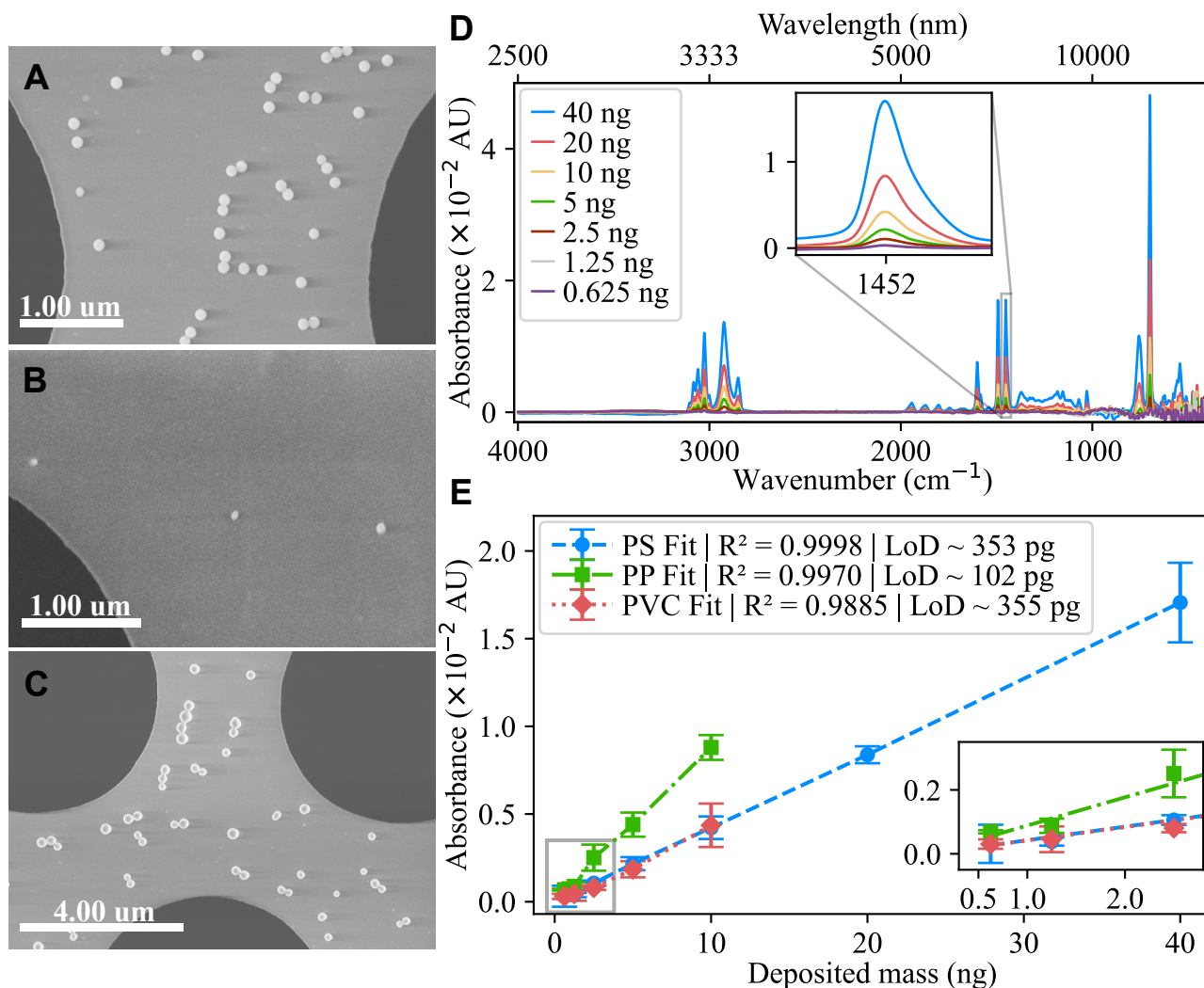


Fig. 2. Characterization and quantification of nanoplastics. (A–C) SEM images of PS, PP, and PVC nanoparticles, respectively. (D) NEMS–FTIR spectra of varying mass loads of PS nanoparticles deposited on the NEMS chips. The inset highlights the 1452 cm^{-1} peak, which was used to construct the calibration curve and determine the LoD. (E) Calibration curves for the 1452 cm^{-1} PS peak, 1377 cm^{-1} PP peak, and 1427 cm^{-1} PVC peak, with the inset showing a zoomed-in view of the region corresponding to lower mass loads (error bars $N=3$, 95% C.L.).

and wavelength [50, 51].

NEMS–FTIR generates spectra comparable to those obtained with transmission–FTIR spectroscopy, allowing seamless integration with existing spectral libraries and chemometric tools for efficient and accurate analysis. Furthermore, since the nanoplastic particles are analyzed under high vacuum, the resulting spectra are free from spectral interferences from water molecules and carbon dioxide.

Fig. 2E shows the calibration curves for PS, PP, and PVC nanoparticles. Calibration curves were constructed using the characteristic peaks

at 1452 cm^{-1} for PS (see inset in Fig. 2D), 1377 cm^{-1} for PP (see inset in Fig. S2), and 1427 cm^{-1} for PVC (see inset in Fig. S3) and the results showed good linearity ($R^2 > 0.9885$). LoDs were calculated from the calibration curves using the relation $3\sigma/m$, where σ is the standard deviation of method blanks ($N = 9$) and m is the slope of the corresponding calibration curve. The results are summarized in Table 1. PP exhibited the steepest calibration slope, resulting from the strongest IR band used for the calibration curve, and consequently had the lowest LoD. Detection limits are lower than those typically achieved by

Table 1. LoD calculation parameters. Summary of the calculated LoDs for different nanoplastics, including the corresponding wavenumbers, standard deviations of the blank (σ) at those wavenumbers ($N = 9$), and calibration slopes (m). LoDs were determined for $3\sigma/m$.

Plastic Type	Wavenumber (cm^{-1})	Standard deviation of the blank (10^{-4} AU)	Slope (10^{-4} AU/ng)	LoD (pg)
PS	1452	0.50	4.25	353
PP	1377	0.30	8.84	102
PVC	1427	0.49	4.17	355

Py-GC/MS [19] and are comparable to the performance of state-of-the-art TD-PTR-MS techniques [21]. The variations in detection limits for different nanoplastic particles did not correlate with nanoparticle size. At higher sample loadings, the observed nanoparticle agglomerations did not result in deviations in linearity.

The mass of PS nanoparticles present on the NEMS chips was estimated using the attenuation coefficient of PS and the absorbances calculated from the NEMS-FTIR spectra at $\tilde{\nu} = 1452 \text{ cm}^{-1}$. The mass estimation procedure is detailed in the "Mass estimation" in the Materials and Methods section. The calculation of the sample absorbance accounted for the spatial distribution of the particles, which predominantly formed a circular patch in the center of the perforation on the NEMS chips. Fig. 3A shows the correlation between the deposited (amount of deposited PS particles) and estimated (from the measured absorbances of PS particles) mass of the nanoplastic particles. The uncertainty on the sample mass deposited on the NEMS chip was estimated from the uncertainty on the tools used for sample preparation and for sample deposition. The largest uncertainty on the sample mass as estimated from the NEMS-FTIR spectra arises from the variability in the measured absorbance $\alpha_s(1452 \text{ cm}^{-1})$. Exact values for the masses deposited on the NEMS chips and estimated masses as calculated from the NEMS-FTIR spectra, along with their standard deviations, can be found in Table S1 in the Supplementary Materials.

Fig. 3B presents a comparison between the NEMS-FTIR spectrum of 20 ng of PS, expressed in absorbance, and a reference spectrum calculated from refractive index data [52] for an equal

sample mass and spot size showing agreement for both peak positions and intensity.

Nanoplastic mixtures

The SEM images in Fig. 4A, B provide the close-up views of the perforated area of the NEMS chip sampled with PS, PP, and PVC nanoparticles previously mixed in a 1:1:1 mass ratio.

The NEMS-FTIR spectrum of the mixture in Fig. 4C shows the characteristic peaks of each polymer component, highlighted by vertical lines. Despite a mass of only 5 ng per component, the peaks corresponding to PS, PP, and PVC are clearly distinguishable. The exact peak positions of the PS, PP, and PVC nanoparticles can be found in the Supplementary Materials, section A. In environmental contexts, where mixtures of different polymer micro- and nanoparticles are commonly encountered, the broad spectral range of NEMS-FTIR increases the likelihood of detecting distinct peaks without interference, facilitating the identification of individual components when their spectral features are sufficiently resolved.

Tea bag leachates

Fig. 5A shows the schematic of the experimental setup for the quantification of nylon tea bag leachates (TBL). The empty tea bag was immersed in 200 mL of preheated water at 95°C for 10 minutes.

Fig. 5B shows micro- and nanoplastic fragments released from the nylon tea bag into the water during standard tea preparation, which were deposited onto the NEMS chip via nanodrop casting. Smaller fragments were also observed on the membranes after sampling the water from the aged tea bags, where a different sampling method, based on aerosolization of the liquid, was used (see Fig. S4).

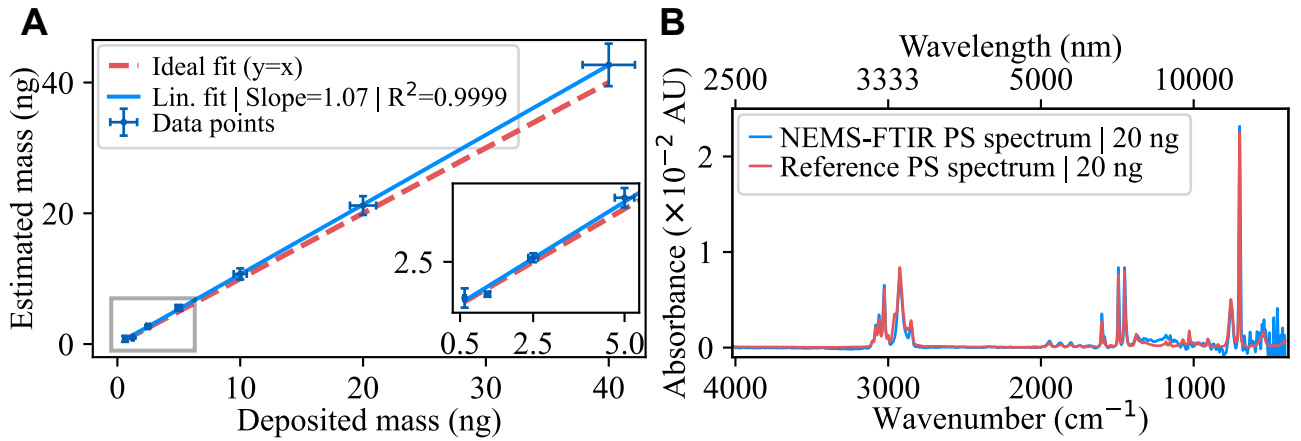


Fig. 3. Quantitative analysis. (A) Correlation between the mass of PS nanoplastic particles deposited on the NEMS chip and the estimated mass derived from the measured NEMS-FTIR spectra after conversion to optical absorbance ($N=3$). The inset highlights the lower mass range for improved visibility. Error bars represent propagated uncertainties from both the measurement and estimation processes. The uncertainty in the IR beam spot size was not included in this analysis and could result in additional error. (B) Absorbance spectrum of 20 ng PS measured via NEMS-FTIR compared to a reference spectrum calculated with Eq. (4) and (7) from PS refractive index data [52].

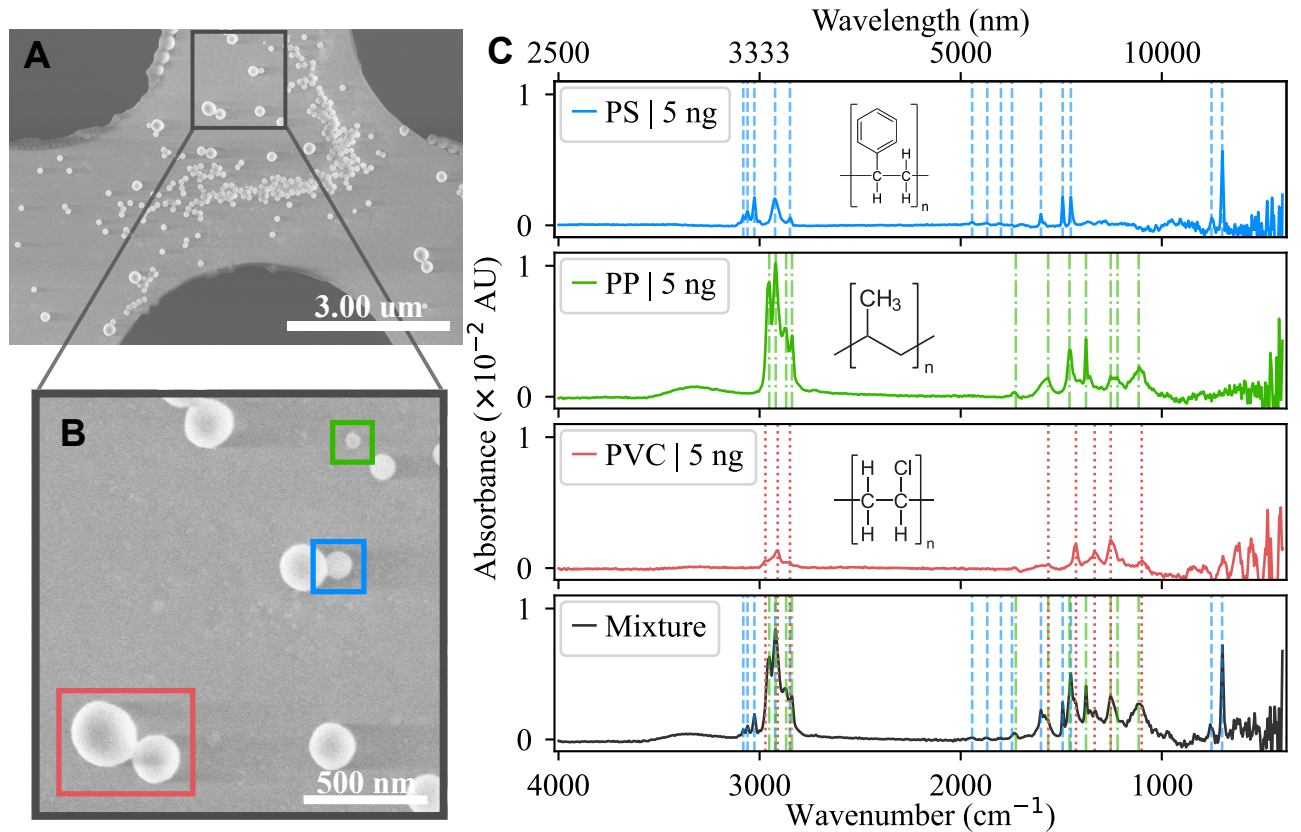


Fig. 4. Characterization of nanoplastic mixture (A) SEM image of a mixture containing PS, PP, and PVC. (B) Magnified view of the membrane area highlighting PS (\varnothing 100 nm, blue square), PP (\varnothing 54 nm, green square), and PVC nanoparticles (\varnothing 262 nm, red square). (C) Stacked spectra of pure PS, PP, and PVC nanoparticles and their 1:1:1 mixture. Vertical lines mark the characteristic peaks of each polymer.

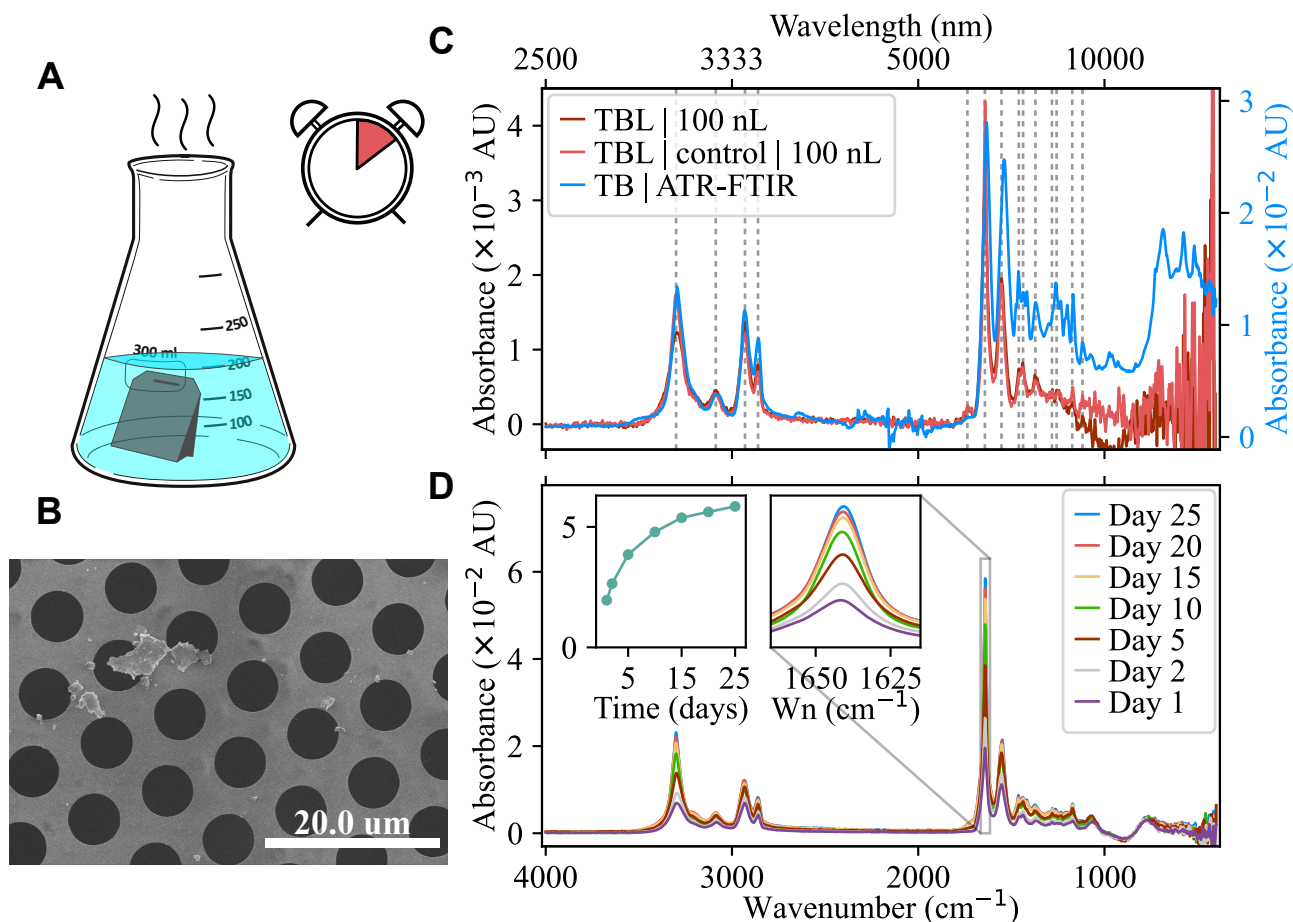


Fig. 5. Characterization of PA particles released from nylon tea bags. (A) Schematic illustrating the sample preparation process. (B) SEM image showing fragments released into water by a nylon tea bag. (C) NEMS-FTIR spectra of nylon tea bag leachates (TBL, 100 nL aliquots deposited onto NEMS chips without pre-concentration) compared to a reference spectrum of the nylon tea bag (TB) recorded by ATR-FTIR (PerkinElmer, 4 cm⁻¹ resolution, 16 scans). Vertical lines indicate characteristic IR peaks associated with PA. (D) NEMS-FTIR spectra of the leachates from a nylon tea bags subjected to accelerated weathering for 25 consecutive days, simulating one year of aging under adjusted conditions. The right inset graph highlights the characteristic PA peak at 1640 cm⁻¹, corresponding to the amide I band. The left inset graph represents the dependence of signal intensity at 1640 cm⁻¹ on the number of days during which the nylon tea bag was subjected to accelerated aging.

Fig. 5C shows the NEMS-FTIR spectra of nylon tea bag leachates prepared in duplicates. A comparison with a reference ATR-FTIR spectrum of the nylon tea bag reveals nearly identical spectral features. Vertical lines highlight characteristic IR peaks corresponding to the chemical structure of PA [49, 53]. Exact peak positions can be found in the Supplementary Materials, section B. The same peaks appear in the NEMS-FTIR spectra of water samples in which individual empty nylon tea bags were immersed and subjected to accelerated aging conditions. As aging progressed, the

nylon tea bags degraded, releasing an increasing amount of PA particles, reflected in the peaks' increasing intensity as shown in the insets (Fig. 5D).

The NEMS-FTIR spectra collected in both cases allowed for chemical identification of the material from which the tea bags were made and confirmation that this material was leaching into the tea water (Fig. 5C, D). The NEMS-FTIR spectra revealed characteristic IR peaks matching well with the literature [53], confirming the presence of PA, including the amide I (1641 cm⁻¹) and amide II (1553 cm⁻¹) bands. The amide I band

primarily arises from C=O stretching vibrations in the amide group, while the amide II band results from a combination of N-H bending and C-N stretching vibrations, which are distinctive features of PA materials.

DISCUSSION

NEMS-FTIR spectroscopy presents a versatile and sensitive platform for detecting micro- and nanoplastics. This approach has the potential to address the growing challenge of plastic pollution and the increasing presence of nanoplastics in consumer products. NEMS-FTIR has demonstrated the ability to detect nanoplastic particles at picogram levels for various plastic materials and nanoparticle sizes. In addition to qualitative characterization, a quantitative analysis was performed. The mass of PS nanoparticles deposited on the NEMS chips was estimated from their measured absorbance, showing good agreement with the expected values. This demonstrates that NEMS-FTIR spectroscopy can provide sensitive detection, identification, and reliable quantification of nanoplastics.

NEMS-FTIR was also applied to detect polymeric particles released from nylon tea bags during tea preparation. The tea bag leachates were deposited directly onto the NEMS chips without prior concentration or filtration. Additionally, nylon tea bags subjected to accelerated aging in water under UV radiation and elevated temperatures were investigated. The intensity of the NEMS-FTIR peaks increased with the number of days of exposure to the artificially created environmental stress, indicating an increased release of polymer particles during aging. This suggests that prolonged exposure to environmental aging conditions significantly contributes to the release of polymeric particles into the surrounding medium. The comparison with online spectral databases, such as Open Specy [54] and Spectragryph [55], and literature, identified the released material as nylon-based PA. In contrast to previous studies [25, 26], which required steeping at least 60 tea bags in 200 mL of water, our approach relies on a single tea bag for the same volume of water, demonstrating higher sensitivity. Here, the untreated leachate was directly deposited onto

NEMS chips without any pre-concentration, and PA particles were detected and identified using NEMS-FTIR.

However, like any analytical technique, NEMS-FTIR has certain limitations. While NEMS-FTIR can be used to detect very small masses of analytes, very dilute solutions do require pre-concentration. The largest droplet volume that can be drop cast on a NEMS chip is limited to approximately 500 nL. Considering a LOD of 353 pg for PS (see Table 1), the minimum detectable concentration of PS is 0.7 $\mu\text{g/mL}$ for a single 500 nL drop of sample. However, in addition to usual pre-concentration techniques such as solid phase extraction, ultrafiltration, and diafiltration, the NEMS-FTIR chip allows new sample pre-concentration possibilities. Multiple droplets can be deposited consecutively on the NEMS chip with intermediate drying steps to increase the analyte mass deposited to the desired level. Sampling via nebulization can also be used to concentrate larger sample volumes onto the NEMS chip as shown for the tea bag leachates. Based on a typical nebulizer flow rate of 20 $\mu\text{L/min}$, a sampling time of 1 hour, and an aerosol capture efficiency of approximately 50 % for 100 nm particles [33], we estimate that concentrations as low as 0.6 ng/mL could be measurable. When dealing with complex matrices containing high concentrations of organic material relative to the target analyte, matrix simplification or removal may be required to remove spectral interferences or avoid overloading the NEMS chip.

One of the key strengths of NEMS-FTIR is its ability to determine the chemical identity of samples with minimal material quantities, independent of particle size, and the possibility for in-situ sample pre-concentration. Its non-destructive nature allows seamless integration with complementary techniques, such as SEM, EDX, or O-PTIR, to gain deeper insights into sample characteristics. Furthermore, it is a cost-effective method that utilizes commercially available FTIR instruments, making it highly accessible for routine monitoring and widespread use. Spectral analysis can be further supported by freely accessible online resources, providing an open-source approach to micro- and nanoplastic identification.

MATERIALS AND METHODS

Nanoplastic particles

PS nanoparticles ($\varnothing 100 \pm 10$ nm, Prod. No. 43302), as a 10 % w/v dispersion in water, were obtained from Sigma–Aldrich (MO, USA). PP ($\varnothing 54$ nm, Prod. No. PP50) and PVC nanoparticles ($\varnothing 262 \pm 30$ nm, Prod. No. PVC250), both as 1 % w/v dispersion in water, were obtained from Lab261 (CA, USA).

Preparation of single and mixed nanoplastic dispersions

All equipment used was first cleaned with acetone (HPLC Plus grade, Prod. No. 650501, Sigma–Aldrich) and isopropyl alcohol (electronic grade, Prod. No. 733458, Sigma–Aldrich), then rinsed five times with distilled deionized water (DDW, 18 M Ω cm; Millipore, MA, USA) followed by UHPLC–MS grade water (Prod. No. W81, Thermo Fisher Scientific, MA, USA). Finally, all items were allowed to dry under a laminar flow hood (Enviroco, NC, USA) to prevent contamination. All samples were prepared in a fume hood (Secuflow, Waldner Holding, Germany) while wearing nitrile gloves (Prod. No. 0439, Helmut Feldtmann GmbH, Germany). Clean nitrile gloves were also used during all experimental procedures.

Serial dilutions and mixture preparation were carried out using UHPLC–MS grade water. A PIPETMAN P1000 micropipette, with matching DIAMOND D1000 TIPACK tips (Prod. No. F144059M and F171500, respectively, Gilson Incorporated, WI, USA), was used for the preparation. All dilutions were stored in hydrolytic class 3 soda–lime glass vials with snap–on lids (Prod. No. LC84.1 and LC87.1, respectively, Carl Roth GmbH, Germany).

All stock and diluted dispersions were first vortexed for 30 seconds using a Mini Vortexer (Heathrow Scientific, IL, USA) to ensure consistent distribution before proceeding with the successive dilution. PS nanoparticle dispersions were prepared at concentrations of 31.25–2000 μ g/mL, while PP and PVC dispersions ranged from 31.25 to 500 μ g/mL. The mixed dispersion of all three types of polymer nanoparticles was prepared in a 1:1:1 mass ratio (PS:PP:PVC). Table 2 summa-

rizes all final concentrations used for each single and mixed sample. Blank samples, consisting of the same UHPLC–MS–grade water used for dilution procedures, underwent the same preparation process as the experimental samples.

Tea bags

Standard tea brewing procedure

The tea bags used in the experiment were purchased online (Temu.com, China), and the procedure for releasing plastic particles from the tea bags was adapted from the study by Hernandez et al. [26]. To minimize potential contamination, the tea bags, made of nylon according to the manufacturer, were purchased empty, eliminating the need for additional cutting or removing the tea leaves. The thin cotton string that attaches a tiny label to the tea bag was carefully removed with scissors. The tea bags were then rinsed five times with UHPLC–MS grade water to avoid impurities or loose plastic particles and allowed to dry overnight in a laminar flow hood.

To simulate a typical tea brewing process, 200 mL of UHPLC–MS grade water was poured into each of two Erlenmeyer flasks (Duran, DWK Life Sciences GmbH, Germany), which had been pre-cleaned following the same procedure described in the "Preparation of single and mixed nanoplastic dispersions" section. Once the water reached its boiling point, the flasks were removed from the hot plate, and a single tea bag was immersed in each. Ten minutes later, the tea bags were carefully removed using clean metal tweezers, and the water was allowed to cool overnight. The flasks were covered with aluminum foil to prevent contamination during the cooling period. Blanks were prepared using the same procedure with the same UHPLC–MS grade water but without tea bags.

Accelerated aging of tea bags

The accelerated aging experiment was carried out in a SimTech Feutron Double Climate Chamber (73 x 77 x 102 cm, Feutron Klimasimulation GmbH, Germany) equipped with two Ultra-Vitalux lamps (300 W, Prod. No. 4008321543929, Osram, Germany) placed 30 cm apart (see Fig. S5 in the Supplementary Materials). These lamps emitted broad-spectrum UV light (UVA: 315–

400 nm, UVB: 280–315 nm) with an irradiance of approximately 59.1 W/m², simulating natural solar radiation to induce degradation.

A metal plate, 32 cm below the lamps, held hydrolytic class 1 soda–lime glass vials with screw caps (Prod. No. LC92.1 and LE03.1, respectively, Carl Roth GmbH, Germany) containing the tea bag samples. The vials allowed good UV transmission, particularly in the UVA range, while minimizing light absorption.

The chamber was operated according to a cyclic schedule: 8 hours of UV exposure at 60°C, followed by 4 hours in the dark at 25°C, mimicking natural day and night temperature fluctuations. This regimen, based on ISO 4892–3 [56] and ASTM G154 [57] standards, lasted 25 days, which is equivalent to approximately one year of natural aging [58]. Seven PA tea bags, each in one glass vial with 30 mL of UHPLC–MS water, were artificially aged, and individual water samples were collected after 1, 2, 5, 10, 15, 20, and 25 day(s) to monitor particle release and degradation. Simultaneously, blanks (water without tea bags) were collected with each respective tea bag sample.

NEMS chips

As shown in Fig. 1A, NEMS chips, or resonators, play a dual role as both sensing devices and sample holders, making them the core of NEMS–FTIR technology. The wafers used in this study to fabricate NEMS chips are made from silicon (Si) and SiN, with thicknesses of 380 μ m and 50 nm, respectively, and an intrinsic tensile stress of approximately 50 MPa for the SiN. After the final manufacturing step, the KOH etching, a 1x1 mm²

SiN membrane is released. This membrane has a perforated area with a diameter of approximately 600 μ m, consisting of 6 μ m holes spaced 3 μ m apart. It acts as the platform on which the sample is deposited for analysis. Two gold electrodes, each 10 μ m wide, are positioned across the chip to enable electrical transduction, allowing mechanical vibrations to be converted into electrical signals, as demonstrated by Bešić et al. [37] and Luhmann et al. [30].

Sampling methods

Nanoliter droplet dispensing

A PIPEJET nanoDispenser (BioFluidix–Hamilton Freiburg, Germany), shown in Fig. S6A, was used to dispense the dispersions on the membrane of the NEMS chips. Polyimide capillaries with an inner diameter of 200 μ m (Prod. No. PJ–20010) were used to deliver individual droplets of 20 nL. A 1 cm length of Tygon tubing (Prod. No. VM–20053–1) was attached to the capillary to facilitate sample loading. The stroke velocity was set to 90 μ m/ms during droplet dispensing.

For each concentration of the dilution series droplets of 20 nL were deposited onto the center of individual NEMS chips. The total deposited mass of each sample is listed in Table 2B. Each deposition was performed in triplicate, with three NEMS chips prepared for each specific polymer mass. Nine blanks were also sampled to provide a reliable baseline for subtraction.

For the mixture of nanoplastic particles, one drop (20 nL) of pre–mixed dispersion was sampled onto a NEMS chip. Three blanks were prepared in parallel.

For the analysis of the tea bag leachates, three

Table 2. Characterization of nanoplastic dispersions. Concentrations of dispersions (A) and total deposited masses of nanoplastic particles (B), differentiating between single– and three–component dispersions. Empty cells indicate concentrations not used in the experiment for the corresponding dispersion.

Nanoplastics type	Concentration (μ g/mL) (A)						
	2000	1000	500	250	125	62.5	31.25
	Total deposited mass (ng) (B)						
PS	40	20	10	5	2.5	1.25	0.625
PP			10	5	2.5	1.25	0.625
PVC			10	5	2.5	1.25	0.625
PS:PP:PVC (1:1:1)				5			

NEMS chips per tea bag (one experimental and one control), were prepared along with three blanks. Rather than sampling a single droplet, each NEMS chip was sequentially loaded with five drops (20 nL each) of tea bag leachates, with a two-minute delay between drops, totaling 100 nL per chip, effectively pre-concentrating the sample.

Aerosolization method for particle deposition

A system incorporating the Portable Aerosol Generation System (PAGS, Handix Scientific Inc., CO, USA) was employed to sample particles released from the nylon tea bags subjected to accelerated weathering cycles. This setup enabled consistent aerosolization and deposition of particles onto the NEMS chips facilitated by the holes in the central region of the membrane. Sampling was conducted at regular intervals (day 1, day 2, day 5, day 10, day 15, day 20, and day 25) to monitor the temporal evolution of particle release. The NEMS chip was placed in a holder (AEROSOL FLOW ADAPTER, Invisible-Light Labs GmbH, Austria), which was then positioned in an eight-channel filter sampler (FILT, Brechtel Manufacturing Inc., CA, USA) equipped with a built-in pump. The pump was set to a flow rate of 0.5 L/min for 5 minutes for each NEMS chip, which allowed sample deposition onto the membranes through the inertial impaction mechanism [33]. Schematic of the setup is presented in Fig. S6B.

Experimental setup

SEM imaging

A Hitachi SU8030 scanning electron microscope (SEM, Hitachi, Japan) was employed to confirm the sizes of the particles deposited on the NEMS chips and to analyze the leachates from the plastic tea bags. For imaging, the NEMS chips were mounted on an aluminum sample holder. Secondary electron (SE) detection in the upper lens mode was utilized to capture high-resolution surface details. The microscope operated at an accelerating voltage of 2 kV with an emission current of 3900 nA. NEMS chips were examined at various magnifications to assess the particle dimensions and the structural characteristics of the deposited material.

NEMS-FTIR spectroscopy

A nanoelectromechanical IR analyzer (EMILIETM, Invisible-Light Labs GmbH, Austria) in conjunction with an FTIR spectrometer (Vertex 70, Bruker Optics, MA, USA), as shown in Fig. 1B, was used to collect all the NEMS-FTIR spectra and confirm the chemical identity of different types of nanoplastic particles, their mixture, and tea bag leachates.

During the measurement process, sampled NEMS chips (Invisible-Light Labs GmbH, Austria) were placed in the vacuum chamber of the nanomechanical IR analyzer at 10^{-5} mbar and the temperature of the chips was consistently regulated to 25°C using the integrated thermoelectric cooling (TEC) controller and Peltier element. A resolution of 4 cm^{-1} , with a stabilization delay of 30 ms, 200 co-additions, and an aperture of 6 mm, were used for the FTIR parameters. The spectral range extended from 4000 to 400 cm^{-1} .

Processing of NEMS-FTIR spectra

All raw NEMS-FTIR spectra were smoothed using a Savitzky-Golay filter with a window length of 20 and a polynomial order of 2. The spectra of the blanks and analytes were then divided by the recorded NEMS-FTIR spectra of the FTIR light source, to account for the wavelength dependent intensity of the light source. The NEMS-FTIR spectrum of the light source was recorded using a NEMS chip coated with a 5 nm ultra-thin Pt film (EMILIETM LIGHT chip, Invisible-Light Labs GmbH, Austria), which acts as a broadband absorber [59].

Spectral calibration was carried out using the intrinsic SiN absorption peak at 835 cm^{-1} as a reference. This calibration was based on transmission measurements through 12 clean, perforated, $2 \times 2\text{ mm}^2$, 50 nm thick low-stress SiN NEMS membranes. Fig. S7 in the Supplementary Materials shows the average transmittance and corresponding absorptance of the NEMS chip's SiN material measured using the internal detector of the FTIR spectrometer (2 mm aperture, 32 scans, and a resolution of 2 cm^{-1}). Despite the different sizes of the membranes ($1 \times 1\text{ mm}^2$ and $2 \times 2\text{ mm}^2$) and perforation areas ($600\text{ }\mu\text{m}$ and $1200\text{ }\mu\text{m}$, respectively), the ratio of perforated to non-perforated membrane material remains

consistent across both membrane types, making the calibration based on the SiN absorption peak possible.

The absorbance for a specific wavenumber $\tilde{\nu}$, $\alpha(\tilde{\nu})$, was calculated from the transmittance $T(\tilde{\nu})$ as $\alpha(\tilde{\nu}) = 1 - T(\tilde{\nu})$, assuming insignificant scattering, yielding $\alpha_{\text{SiN}}(835 \text{ cm}^{-1}) = 0.21 \pm 0.01$. The NEMS-FTIR response of the bare SiN chip, R_{SiN} , was then related to absorbance through a calibration factor β :

$$\beta = \frac{\alpha_{\text{SiN}}(835 \text{ cm}^{-1})}{R_{\text{SiN}}(835 \text{ cm}^{-1})}. \quad (1)$$

Depositing the nanoplastics on the membrane with the nanodropper created a circular sample spot (see Fig. S1 in Supplementary Materials). The nanoplastics occupied the area Σ_S , which is smaller than the area of the IR beam illuminating the chip, Σ_{IR} . Furthermore, the increased photothermal response, if the sample is concentrated in the membrane center instead of being evenly distributed over the entire membrane, was corrected by γ [60]. The sample absorbance $\alpha_S(\tilde{\nu})$ can now be calculated from the measured NEMS-FTIR signal of the sample, R_S , as:

$$\alpha_S(\tilde{\nu}) = \beta R_S(\tilde{\nu}) \frac{\Sigma_{\text{IR}}}{\Sigma_S} \frac{1}{\gamma}. \quad (2)$$

Σ_{IR} can be calculated from the reflective focal length ratio of the FTIR spectrometer and EMILIETM optics, which here was 25 mm/160 mm ≈ 0.156 . The resulting IR beam diameter on the NEMS chip is then given by $d_{\text{beam}} = 0.156 \cdot d_{\text{aperture}}$. For the aperture of 6 mm, used in all experiments, the IR beam diameter on the chip is approximately $d_{\text{IR}} = 0.94 \text{ mm}$. The total area illuminated by the IR beam can be calculated as $\Sigma_{\text{IR}} = \pi(d_{\text{IR}}/2)^2 - \Sigma_P$, with the area of the perforation $\Sigma_P = 0.108 \text{ mm}^2$.

Σ_S corresponds to the diameter of the central nanoplastics area on the membrane with a diameter of $d_S = 504 \pm 46 \text{ }\mu\text{m}$, based on six independent measurements. The total sample area is then given by $\Sigma_S = \eta \pi (d_S/2)^2$, with the fill factor of the perforation $\eta = 0.62$.

γ was calculated by finite element method (FEM) simulations by Kanellopoulos et al. [61].

The results for a square low-stress SiN membrane with a side length of 1 mm are given in Fig. S8 in the Supplementary Materials, yielding $\gamma = 1.68 \pm 0.05$ for the given sample spot size. The nanoplastics spots on the membrane formed a coffee ring, as seen in (see Fig. S1 in the Supplementary Materials). Up to 90% of particles typically accumulate at the droplet perimeter in the coffee ring, as shown for nanometer-sized PS dispersions [62, 63]. FEM simulations have shown that the formation of a coffee ring has no significant effect on the NEMS-FTIR response.

Finally, the blank-corrected nanoplastic absorbance can be calculated from

$$A(\tilde{\nu}) = -\log_{10}(1 - [\alpha_S(\tilde{\nu}) - \alpha_B(\tilde{\nu})]), \quad (3)$$

with the absorbance of the blank $\alpha_B(\tilde{\nu})$.

Mass estimation

This framework aims to estimate the actual mass of the nanoplastic on the NEMS chip responsible for the NEMS-FTIR signal. Following the approach of Dudani and Takahama [64], it was assumed that particle scattering is negligible compared to absorption; thus, correction factors related to scattering are not required. Particles are much smaller than the wavelength of IR radiation used in this study, placing them in the Rayleigh regime, where absorption dominates IR attenuation. In this case, the absorbance $A(\tilde{\nu})$ of the deposited particles can be expressed as a function of the linear attenuation coefficient $\mu_{10}(\tilde{\nu})$:

$$A(\tilde{\nu}) = \mu_{10}(\tilde{\nu}) h_{\text{eff}} = \mu_{10}(\tilde{\nu}) \frac{m}{\rho \Sigma_S}, \quad (4)$$

where the effective film thickness h_{eff} is expressed as a function of the analyte mass m , the nanoparticle material density ρ , and the sample area Σ_S .

In NEMS-FTIR, the measured absorbance values are small ($\alpha_S(\tilde{\nu}) \ll 1$) and the absorbance (3) can be approximated using a first-order Taylor series expansion:

$$A(\tilde{\nu}) \approx \frac{\alpha_S(\tilde{\nu}) - \alpha_B(\tilde{\nu})}{\ln(10)}. \quad (5)$$

Combining Eqs. (2), (4), (5), and solving for the analyte mass gives:

$$m = \beta \frac{R_S(\tilde{\nu}) - R_B(\tilde{\nu})}{\mu_{10}(\tilde{\nu})} \frac{\rho}{\ln(10)} \frac{\Sigma_{\text{IR}}}{\gamma}, \quad (6)$$

where $R_B(\tilde{\nu})$ is the NEMS–FTIR response of the averaged blank spectra, and $\tilde{\nu}$ denotes the wavenumber corresponding to a characteristic vibrational mode of the sample.

The attenuation coefficients of the substance are determined from its complex refractive index, defined as $\tilde{n} = n + ik$, where n and k are the real and imaginary components, respectively. In the electrostatic approximation [65], the volume attenuation coefficient for small particles depends on the wavenumber and the refractive index of the substance forming the particles [66]:

$$\mu_{10}(\tilde{\nu}) = \frac{6\pi\tilde{\nu}}{\ln(10)} \operatorname{Im} \left\{ \frac{\tilde{n}^2(\tilde{\nu}) - 1}{\tilde{n}^2(\tilde{\nu}) + 2} \right\}. \quad (7)$$

Supplementary Materials

This PDF file includes:

Supplementary Text

Figs.S1 to S8

Table S1

REFERENCES

- [1] L. Dick, P. R. Batista, P. Zaby, G. Manhart, V. Kopatz, L. Kogler, V. Pichler, F. Grebien, V. Bakos, B. G. Plósz, *et al.*, “The adsorption of drugs on nanoplastics has severe biological impact,” *Scientific Reports*, vol. 14, no. 1, p. 25853, 2024.
- [2] L. A. Amaral-Zettler, E. R. Zettler, and T. J. Mincer, “Ecology of the plastisphere,” *Nature Reviews Microbiology*, vol. 18, no. 3, pp. 139–151, 2020.
- [3] A. A. Koelmans, E. Besseling, and E. M. Foekema, “Leaching of plastic additives to marine organisms,” *Environmental pollution*, vol. 187, pp. 49–54, 2014.
- [4] S. L. Wright, R. C. Thompson, and T. S. Galloway, “The physical impacts of microplastics on marine organisms: a review,” *Environmental pollution*, vol. 178, pp. 483–492, 2013.
- [5] L. Wang, W.-M. Wu, N. S. Bolan, D. C. Tsang, Y. Li, M. Qin, and D. Hou, “Environmental fate, toxicity and risk management strategies of nanoplastics in the environment: Current status and future perspectives,” *Journal of hazardous materials*, vol. 401, p. 123415, 2021.
- [6] O. H. Fred-Ahmadu, G. Bhagwat, I. Oluyoye, N. U. Benson, O. O. Ayejuyo, and T. Palanisami, “Interaction of chemical contaminants with microplastics: Principles and perspectives,” *Science of the Total Environment*, vol. 706, p. 135978, 2020.
- [7] A. A. Horton and S. J. Dixon, “Microplastics: An introduction to environmental transport processes,” *Wiley Interdisciplinary Reviews: Water*, vol. 5, no. 2, p. e1268, 2018.
- [8] N. Ali, J. Katsouli, E. L. Marczylo, T. W. Gant, S. Wright, and J. B. de la Serna, “The potential impacts of micro-and-nano plastics on various organ systems in humans,” *eBioMedicine*, vol. 99, 2024.
- [9] A. K  ppler, D. Fischer, S. Oberbeckmann, G. Schernewski, M. Labrenz, K.-J. Eichhorn, and B. Voit, “Analysis of environmental microplastics by vibrational microspectroscopy: Ftir, raman or both?,” *Analytical and Bioanalytical Chemistry*, vol. 408, pp. 8377–8391, Nov 2016.
- [10] S. Adhikari, V. Kelkar, R. Kumar, and R. U. Halden, “Methods and challenges in the detection of microplastics and nanoplastics: a mini-review,” *Polymer International*, vol. 71, no. 5, pp. 543–551, 2022.
- [11] J. Caldwell, P. Taladriz-Blanco, R. Lehner, A. Lubskyy, R. D. Ortuso, B. Rothen-Rutishauser, and A. Petri-Fink, “The micro-, submicron-, and nanoplastic hunt: A review of detection methods for plastic particles,” *Chemosphere*, vol. 293, p. 133514, 2022.
- [12] X.-X. Zhou, R. Liu, L.-T. Hao, and J.-F. Liu, “Identification of polystyrene nanoplastics using surface enhanced raman spectroscopy,” *Talanta*, vol. 221, p. 121552, 2021.

- [13] R. Hu, K. Zhang, W. Wang, L. Wei, and Y. Lai, "Quantitative and sensitive analysis of polystyrene nanoplastics down to 50 nm by surface-enhanced raman spectroscopy in water," *Journal of Hazardous Materials*, vol. 429, p. 128388, 2022.
- [14] K. Duswald, V. Pichler, V. Kopatz, T. Limberger, V. Karl, D. Wimberger, R. Zimmerleiter, W. Wadsak, M. Hettich, L. Kenner, *et al.*, "Detection of unlabeled micro-and nanoplastics in unstained tissue with optical photothermal infrared spectroscopy," *bioRxiv*, pp. 2024–11, 2024.
- [15] Y. Su, X. Hu, H. Tang, K. Lu, H. Li, S. Liu, B. Xing, and R. Ji, "Steam disinfection releases micro (nano) plastics from silicone-rubber baby teats as examined by optical photothermal infrared microspectroscopy," *Nature Nanotechnology*, vol. 17, no. 1, pp. 76–85, 2022.
- [16] H. Cai, E. G. Xu, F. Du, R. Li, J. Liu, and H. Shi, "Analysis of environmental nanoplastics: Progress and challenges," *Chemical Engineering Journal*, vol. 410, p. 128208, 2021.
- [17] E. D. Okoffo and K. V. Thomas, "Quantitative analysis of nanoplastics in environmental and potable waters by pyrolysis-gas chromatography–mass spectrometry," *Journal of Hazardous Materials*, vol. 464, p. 133013, 2024.
- [18] Y. Xu, Q. Ou, M. Jiao, G. Liu, and J. P. Van Der Hoek, "Identification and quantification of nanoplastics in surface water and ground-water by pyrolysis gas chromatography–mass spectrometry," *Environmental Science & Technology*, vol. 56, no. 8, pp. 4988–4997, 2022.
- [19] H. Li, L. M. Lee, D. Yu, S. H. Chan, and A. Li, "An optimized multi-technique based analytical platform for identification, characterization and quantification of nanoplastics in water," *Talanta*, vol. 272, p. 125800, 2024.
- [20] Y. Li, C. Zhang, Z. Tian, X. Cai, and B. Guan, "Identification and quantification of nanoplastics (20–1000 nm) in a drinking water treatment plant using afm-ir and pyr-gc/ms," *Journal of Hazardous Materials*, vol. 463, p. 132933, 2024.
- [21] D. Materić, A. Kasper-Giebl, D. Kau, M. Anten, M. Greilinger, E. Ludewig, E. van Seville, T. Röckmann, and R. Holzinger, "Micro- and nanoplastics in alpine snow: A new method for chemical identification and (semi)quantification in the nanogram range," *Environmental Science & Technology*, vol. 54, no. 4, pp. 2353–2359, 2020. PMID: 31951124.
- [22] A. Foetisch, M. Filella, B. Watts, L.-H. Vinot, and M. Bigalke, "Identification and characterisation of individual nanoplastics by scanning transmission x-ray microscopy (stxm)," *Journal of hazardous materials*, vol. 426, p. 127804, 2022.
- [23] K. Kniazev, I. M. Pavlovetc, S. Zhang, J. Kim, R. L. Stevenson, K. Doudrick, and M. Kuno, "Using infrared photothermal heterodyne imaging to characterize micro-and nanoplastics in complex environmental matrices," *Environmental Science & Technology*, vol. 55, no. 23, pp. 15891–15899, 2021.
- [24] T. Mei, J. Wang, X. Xiao, J. Lv, Q. Li, H. Dai, X. Liu, and F. Pi, "Identification and evaluation of microplastics from tea filter bags based on raman imaging," *Foods*, vol. 11, no. 18, p. 2871, 2022.
- [25] G. Banaei, D. Abass, A. Tavakolpournegari, J. Martín-Pérez, J. Gutiérrez, G. Peng, T. Reemtsma, R. Marcos, A. Hernández, and A. García-Rodríguez, "Teabag-derived micro/nanoplastics (true-to-life mnpls) as a surrogate for real-life exposure scenarios," *Chemosphere*, vol. 368, p. 143736, 2024.
- [26] L. M. Hernandez, E. G. Xu, H. C. Larsson, R. Tahara, V. B. Maisuria, and N. Tufenkji, "Plastic teabags release billions of microparticles and nanoparticles into tea," *Environ-*

- mental science & technology*, vol. 53, no. 21, pp. 12300–12310, 2019.
- [27] E. Commission, J. R. Centre, O. Geiss, S. Belz, C. Cella, D. Gilliland, R. La Spina, D. Méhn, and B. Sokull-Klüttgen, *Analytical methods to measure microplastics in drinking water – Review and evaluation of methods*. Publications Office of the European Union, 2024.
- [28] J. Zhang, D. Fu, H. Feng, Y. Li, S. Zhang, C. Peng, Y. Wang, H. Sun, and L. Wang, “Mass spectrometry detection of environmental microplastics: Advances and challenges,” *TrAC Trends in Analytical Chemistry*, vol. 170, p. 117472, 2024.
- [29] J. Xie, A. Gowen, W. Xu, and J. Xu, “Analysing micro- and nanoplastics with cutting-edge infrared spectroscopy techniques: a critical review,” *Anal. Methods*, vol. 16, pp. 2177–2197, 2024.
- [30] N. Luhmann, R. G. West, J. P. Lafleur, and S. Schmid, “Nanoelectromechanical infrared spectroscopy with in situ separation by thermal desorption: Nems-ir-td,” *ACS Sensors*, vol. 8, no. 4, pp. 1462–1470, 2023. PMID: 37067504.
- [31] M. Kurek, M. Carnoy, P. E. Larsen, L. H. Nielsen, O. Hansen, T. Rades, S. Schmid, and A. Boisen, “Nanomechanical infrared spectroscopy with vibrating filters for pharmaceutical analysis,” *Angewandte Chemie*, vol. 129, no. 14, pp. 3959–3963, 2017.
- [32] R. G. West, K. Kanellopoulos, and S. Schmid, “Photothermal microscopy and spectroscopy with nanomechanical resonators,” *The Journal of Physical Chemistry C*, vol. 127, no. 45, pp. 21915–21929, 2023.
- [33] S. Schmid, M. Kurek, J. Q. Adolphsen, and A. Boisen, “Real-time single airborne nanoparticle detection with nanomechanical resonant filter-fiber,” *Scientific reports*, vol. 3, no. 1, p. 1288, 2013.
- [34] H. Bešić, A. Demir, J. Steurer, N. Luhmann, and S. Schmid, “Schemes for tracking resonance frequency for micro-and nanomechanical resonators,” *Physical Review Applied*, vol. 20, no. 2, p. 024023, 2023.
- [35] H. Bešić, A. Demir, V. Vukićević, J. Steurer, and S. Schmid, “Adaptable frequency counter with phase filtering for resonance frequency monitoring in nanomechanical sensing,” *IEEE Sensors Journal*, 2024.
- [36] S. Yamada, S. Schmid, T. Larsen, O. Hansen, and A. Boisen, “Photothermal infrared spectroscopy of airborne samples with mechanical string resonators,” *Analytical chemistry*, vol. 85, no. 21, pp. 10531–10535, 2013.
- [37] H. Bešić, A. Deutschmann-Olek, K. Mešić, K. Kanellopoulos, and S. Schmid, “Optimized signal estimation in nanomechanical photothermal sensing via thermal response modeling and kalman filtering,” *IEEE Sensors Journal*, vol. 24, no. 19, pp. 30264–30274, 2024.
- [38] F. Samaeifar, A. C. Ceccacci, S. B. Goswami, L. H. Nielsen, A. Affi, K. Zór, and A. Boisen, “Evaluation of the solid state form of tadalafil in sub-micron thin films using nanomechanical infrared spectroscopy,” *International Journal of Pharmaceutics*, vol. 565, pp. 227–232, 2019.
- [39] A. J. Andersen, S. Yamada, E. Pramodkumar, T. L. Andresen, A. Boisen, and S. Schmid, “Nanomechanical ir spectroscopy for fast analysis of liquid-dispersed engineered nanomaterials,” *Sensors and Actuators B: Chemical*, vol. 233, pp. 667–673, 2016.
- [40] A. Casci Ceccacci, A. Cagliani, P. Marizza, S. Schmid, and A. Boisen, “Thin film analysis by nanomechanical infrared spectroscopy,” *ACS omega*, vol. 4, no. 4, pp. 7628–7635, 2019.
- [41] T. Biswas, N. Miriyala, C. Doolin, X. Liu, T. Thundat, and J. Davis, “Femtogram-

- scale photothermal spectroscopy of explosive molecules on nanostrings,” *Analytical chemistry*, vol. 86, no. 22, pp. 11368–11372, 2014.
- [42] L. Tetard, A. Passian, R. H. Farahi, B. H. Davison, and T. Thundat, “Optomechanical spectroscopy with broadband interferometric and quantum cascade laser sources,” *Optics letters*, vol. 36, no. 16, pp. 3251–3253, 2011.
- [43] M. Zając, J. Kotyńska, M. Worobiczuk, J. Breczko, and M. Naumowicz, “The effect of submicron polystyrene on the electrokinetic potential of cell membranes of red blood cells and platelets,” *Membranes*, vol. 12, p. 366, 03 2022.
- [44] B. Wu, X. Wu, S. Liu, Z. Wang, and L. Chen, “Size-dependent effects of polystyrene microplastics on cytotoxicity and efflux pump inhibition in human caco-2 cells,” *Chemosphere*, vol. 221, pp. 333–341, 2019.
- [45] B. Smith, “The infrared spectra of polymers iii: Hydrocarbon polymers,” *Spectroscopy*, vol. 36, pp. 22–25, 2021.
- [46] T. L. Myers, R. G. Tonkyn, A. M. Oeck, T. O. Danby, J. S. Loring, M. S. Taubman, S. W. Sharpe, J. C. Birnbaum, and T. J. Johnson, “Tarpa / pnnl liquid phase ir spectra,” 2025. (retrieved January 24, 2025).
- [47] M. Beltran and A. Marcilla, “Fourier transform infrared spectroscopy applied to the study of pvc decomposition,” *European polymer journal*, vol. 33, no. 7, pp. 1135–1142, 1997.
- [48] R. R. Stromberg, S. Straus, and B. Achhammer, “Infrared spectra of thermally degraded poly (vinyl chloride),” *Journal of Research of the National Bureau of Standards*, vol. 60, no. 2, pp. 147–152, 1958.
- [49] A. S. Tagg, J. P. Harrison, Y. Ju-Nam, M. Sapp, E. L. Bradley, C. J. Sinclair, and J. J. Ojeda, “Fenton’s reagent for the rapid and efficient isolation of microplastics from wastewater,” *Chemical Communications*, vol. 53, no. 2, pp. 372–375, 2017.
- [50] M. Bradley, “Pathlength considerations with atr sampling in ftir,” *American Laboratory*, vol. 60, no. 7, pp. 20–22, 2018.
- [51] T. Mayerhofer and C. Krafft, “Five reasons why not every peak shift in infrared (ir) spectra indicates a chemical structure change,” *Spectroscopy Supplements*, 2021.
- [52] T. L. Myers et al., “Accurate measurement of the optical constants n and k for a series of 57 inorganic and organic liquids for optical modeling and detection,” *Appl. Spectrosc.*, vol. 72, no. 4, pp. 535–550, 2018.
- [53] B. Smith, “Infrared spectroscopy of polymers, xi: Introduction to organic nitrogen polymers,” *Spectroscopy*, vol. 38, pp. 14–18, 2023.
- [54] W. Cowger, Z. Steinmetz, A. Gray, K. Munno, J. Lynch, H. Hapich, S. Primpke, H. De Frond, C. Rochman, and O. Herodotou, “Microplastic spectral classification needs an open source community: open specy to the rescue!,” *Analytical chemistry*, vol. 93, no. 21, pp. 7543–7548, 2021.
- [55] F. Menges, “Spectragryph optical spectroscopy software, version 1.2.16.1.” <http://www.effemm2.de/spectragryph/>. Accessed: 2025-02-27.
- [56] I. O. for Standardization, “Plastics — methods of exposure to laboratory light sources — part 3: Fluorescent uv lamps,” Tech. Rep. ISO 4892-3, International Organization for Standardization, Geneva, Switzerland, 2016.
- [57] A. International, “Standard practice for operating fluorescent ultraviolet (uv) lamp apparatus for exposure of nonmetallic materials,” Tech. Rep. ASTM G154, ASTM International, West Conshohocken, PA, 2020.

- [58] M. Philip and F. Al-Azzawi, “Effects of natural and artificial weathering on the physical properties of recycled poly (ethylene terephthalate),” *Journal of Polymers and the Environment*, vol. 26, no. 8, pp. 3139–3148, 2018.
- [59] M. Piller, J. Hiesberger, E. Wistrela, P. Martini, N. Luhmann, and S. Schmid, “Thermal ir detection with nanoelectromechanical silicon nitride trampoline resonators,” *IEEE Sensors Journal*, vol. 23, no. 2, pp. 1066–1071, 2022.
- [60] S. Schmid, L. G. Villanueva, and M. L. Roukes, *Fundamentals of nanomechanical resonators, 2nd Edition*. Nature Springer, 2023.
- [61] K. Kanellopoulos, F. Ladinig, S. Emminger, P. Martini, R. G. West, and S. Schmid, “Comparative analysis of nanomechanical resonators: sensitivity, response time, and practical considerations in photothermal sensing,” *Microsystems & Nanoengineering*, vol. 11, no. 1, p. 28, 2025.
- [62] Y. Li, Q. Yang, M. Li, and Y. Song, “Rate-dependent interface capture beyond the coffee-ring effect,” *Scientific reports*, vol. 6, no. 1, p. 24628, 2016.
- [63] M. Rey, J. Walter, J. Harrer, C. M. Perez, S. Chiera, S. Nair, M. Ickler, A. Fuchs, M. Michaud, M. J. Uttinger, *et al.*, “Versatile strategy for homogeneous drying patterns of dispersed particles,” *Nature Communications*, vol. 13, no. 1, p. 2840, 2022.
- [64] N. Dudani and S. Takahama, “Design and fabrication of an electrostatic precipitator for infrared spectroscopy,” *Atmospheric Measurement Techniques Discussions*, vol. 2022, pp. 1–25, 2022.
- [65] H. C. Hulst and H. C. van de Hulst, *Light scattering by small particles*. Courier Corporation, 1981.
- [66] D. R. H. Craig F. Bohren, *Absorption and Scattering of Light by Small Particles*. John Wiley & Sons, Ltd, 1998.

Acknowledgements

We sincerely thank Jürgen Smoliner, Alois Lugstein and Masiar Sistani from the Institute of Solid State Electronics at TU Wien for letting us use their FTIR spectrometer. We thank Michael Schneider and Paolo Martini from the Institute of Sensor and Actuator Systems at TU Wien for acquiring the SEM images and helping with finite element method simulations, respectively. Special thanks go to the Invisible–Light Labs team for their technical expertise and supportive encouragement, as well as to our colleagues from the MNS group at TU Wien (Institute of Sensor and Actuator Systems) for their valuable insights and collaboration. We also gratefully acknowledge Georg Pfusterschmied for providing the image in Fig. 1A and Mihnea Surdu from the Extreme Environments Research Laboratory at EPFL in Switzerland for his assistance with the aerosol sampling setup.

Funding: This project received funding from the European Commission under grant agreement HORIZON–EIC–2021–TRANSITIONOPEN–101058011 – NEMILIES, the Austria Wirtschaftsservice (AWS SEED, Deep Tech & Physical Sciences project P2422873), the Austrian Science Fund (FWF) under project I 6086–N, and the Novo Nordisk Foundation under grant number NNF22OC0077964 – MAS-MONADE.

Author contributions:

Conceptualization: JTP, JPL, and SS. Methodology: JTP, JH, EŠ, NL, HB, JPL, and SS. Investigation: JTP, JH, EŠ, NL, AG, and HB. Supervision: AG, JPL, and SS. Writing—original draft: JTP and EŠ. Writing—review & editing: JTP, JPL, NL, JH and SS.

Competing interests: NL, HB, JPL, and SS are co-founders of Invisible–Light Labs GmbH who provided the analytical instrumentation used in this study. JTP, NL, and JH are employed by Invisible–Light Labs GmbH. EŠ and AG declare no competing interests.

Supplementary Materials for **Nanoplastic Analysis with Nanoelectromechanical System Fourier Transform Infrared Spectroscopy: NEMS–FTIR**

Jelena Timarac–Popović^{1,2*}, Johannes Hiesberger^{1,2}, Eldira Šesto¹, Niklas Luhmann²,
Ariane Giesriegl¹, Hajrudin Bešić¹, Josiane P. Lafleur², and Silvan Schmid^{1*}

¹*TU Wien, Institute of Sensor and Actuator Systems, Gusshausstrasse 27–29, 1040 Vienna, Austria.*

²*Invisible–Light Labs GmbH, Taubstummengasse 11, 1040 Vienna, Austria.*

(Dated: April 18, 2025)

This PDF file includes:

Supplementary Text
Figs. S1 to S8
Table S1

*Correspondence e–mail address: jelena.popovic@tuwien.ac.at, silvan.schmid@tuwien.ac.at

A. NEMS–FTIR spectra of single NPs

The vertical lines observed in the NEMS–FTIR spectra (visible on Fig. 4C) correspond to characteristic wavenumbers associated with specific nanoplastic particles. Some lines correspond to potential minor oxidation or contamination during sample preparation.

The NEMS–FTIR spectrum of PS nanoparticles exhibit vertical lines at the following wavenumbers: 700, 753, 1452, 1493, 1601, 1745, 1800, 1868, 1943, 2849, 2923, 3026, 3060, and 3081 cm^{-1} .

The NEMS–FTIR spectrum of PP nanoparticles exhibit vertical lines at the following wavenumbers: 1115, 1220, 1254, 1377, 1459, 1565, 1726, 2839, 2868, 2920, and 2952 cm^{-1} .

The NEMS–FTIR spectrum of PVC nanoparticles exhibit vertical lines at the following wavenumbers: 1100, 1254, 1334, 1427, 1564, 2849, 2910, and 2971 cm^{-1} .

B. NEMS–FTIR spectra of tea bag leachates

The NEMS–FTIR spectra of tea bag leachates (see Fig. 5C) exhibit vertical lines at the following wavenumbers: 1118, 1173, 1257, 1282, 1371, 1437, 1460, 1553, 1642, 1736, 2860, 2930, 3087, and 3300 cm^{-1} .

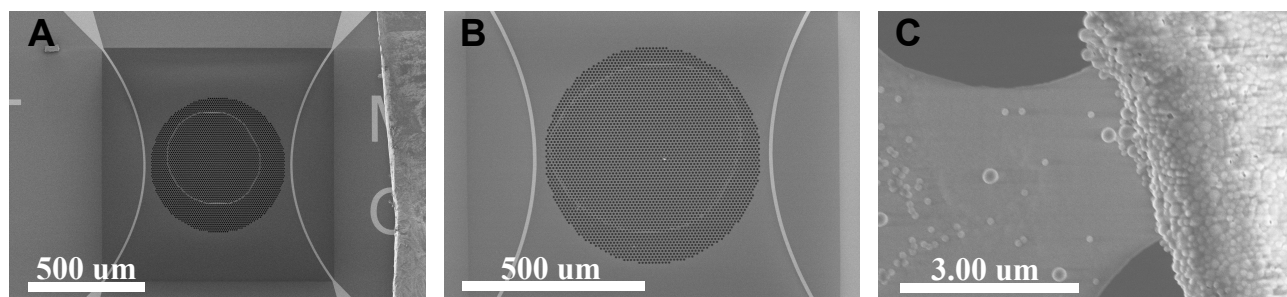


Fig. S1. Coffee ring effect. SEM image of (A) 1.25 ng of PP nanoparticles, (B) 1.25 ng of PS nanoparticles, (C) a PS-PP-PVC mixture mixed in a mass ratio of 1:1:1, containing 5 ng of each component. Image (C) also shows a close-up view of the coffee ring structure.

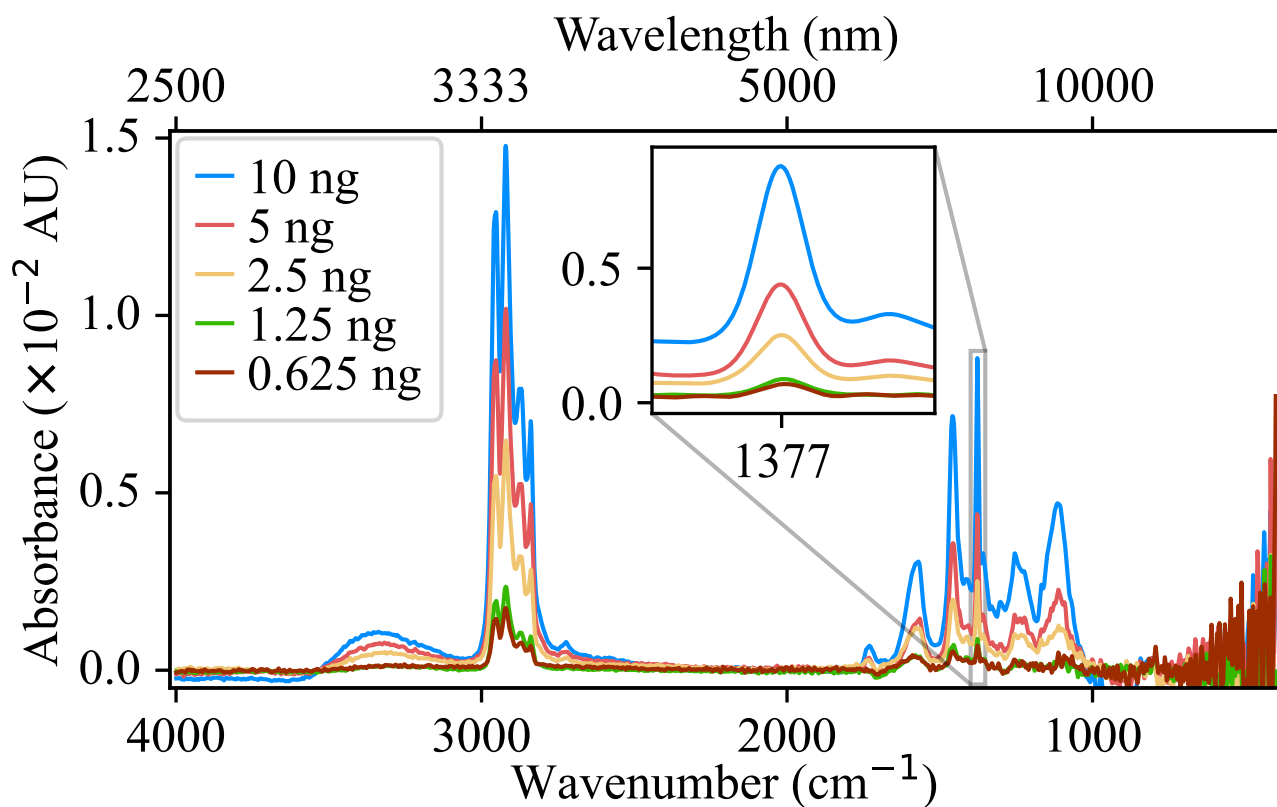


Fig. S2. Characterization of PP nanoplastics. NEMS-FTIR spectra of PP nanoplastics deposited on NEMS chips at varying mass loads. The inset highlights the 1377 cm^{-1} peak, which was used to construct the calibration curve and determine the LoD.

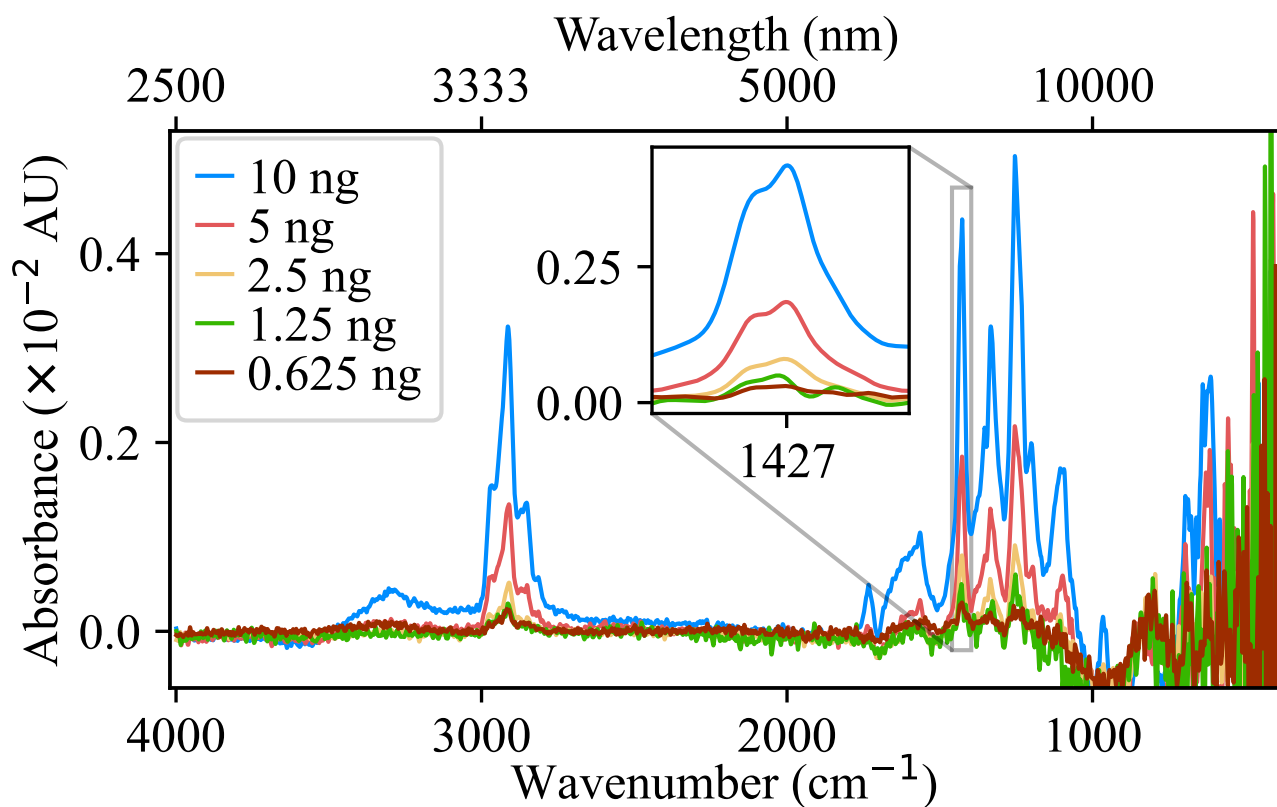


Fig. S3. Characterization of PVC nanoplastics. NEMS-FTIR spectra of PVC nanoplastics deposited on NEMS chips at varying mass loads. The inset highlights the 1427 cm^{-1} peak, which was used to construct the calibration curve and determine the LoD.

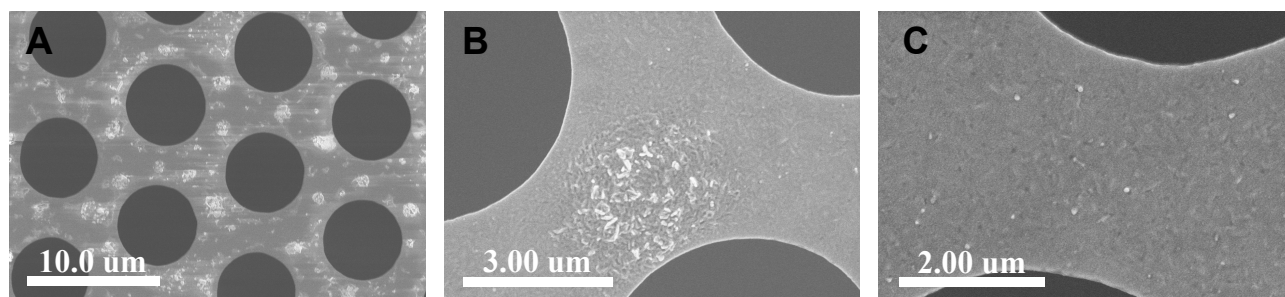


Fig. S4. Micro- and nanofragments released by tea bags during accelerated aging. (A–C) Magnified views of the membrane sampled with water in which a tea bag had been soaked for 15 days and exposed to environmental stress.



Fig. S5. Experimental setup for the accelerated aging of tea bags. The setup includes a controlled environment chamber for simulating environmental stress through cyclic exposure to elevated temperature and UV radiation, with tea bags immersed in water for the duration of the experiment.

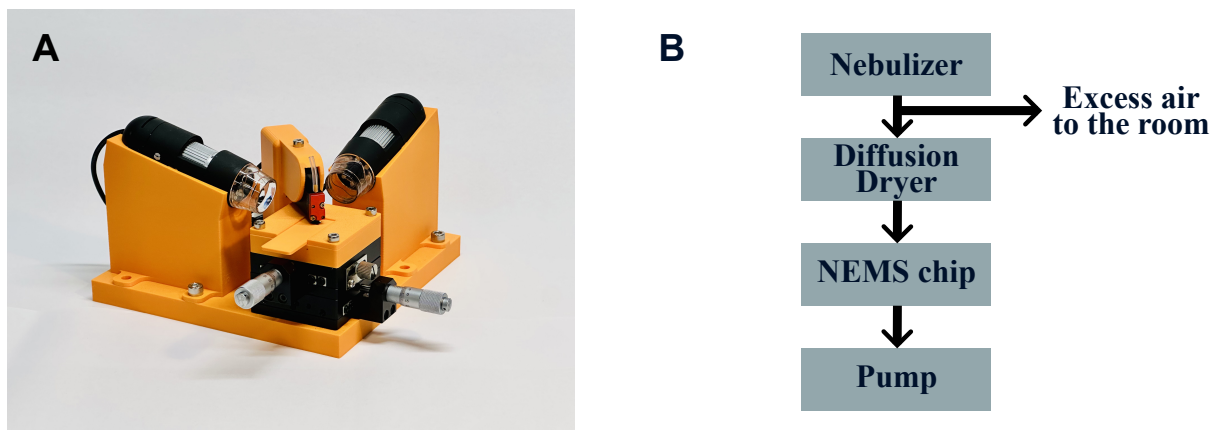


Fig. S6. Sampling setups. (A) The PIPEJET nanoDispenser, equipped with two cameras and an XY stage, enables precise positioning of the NEMS chips beneath the dispensing capillary for accurate droplet deposition onto the membrane. (B) Schematic representation of the setup, comprising a nebulizer (Portable Aerosol Generation System, PAGS, Handix Scientific Inc., CO, USA) for aerosolizing the liquid into fine droplets, a diffusion dryer (DDU, 570/L, Topas GmbH, Germany), and a NEMS chip holder (Aerosol Flow Adapter, Invisible-Light Labs GmbH, Austria) containing the NEMS chip. The chip holder was placed in an eight-channel filter sampler (FILT, Brechtel Manufacturing Inc., CA, USA), which includes a built-in pump. The sampling flow rate was set to 0.5 L/min for a duration of 5 minutes for each NEMS chip. Sampling is based on the inertial impaction deposition mechanism.

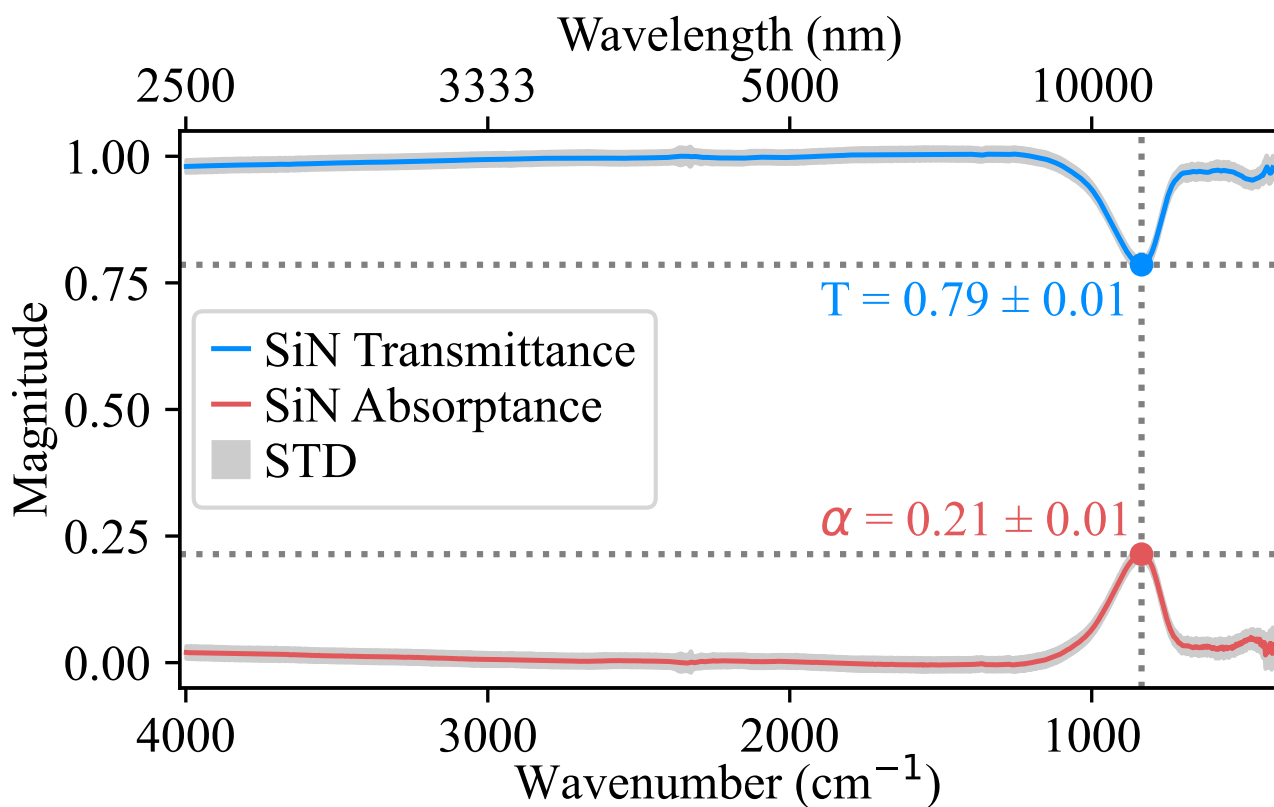


Fig. S7. IR spectral features of SiN membranes. Average transmittance and absorptance spectra of 12 individual empty NEMS chips composed of 50 nm thick low-stress SiN. The shaded regions represent the standard deviations associated with each spectrum. The dashed vertical line at 835 cm⁻¹ marks the characteristic SiN peak, where the transmittance and absorptance values, along with their standard deviations, were evaluated.

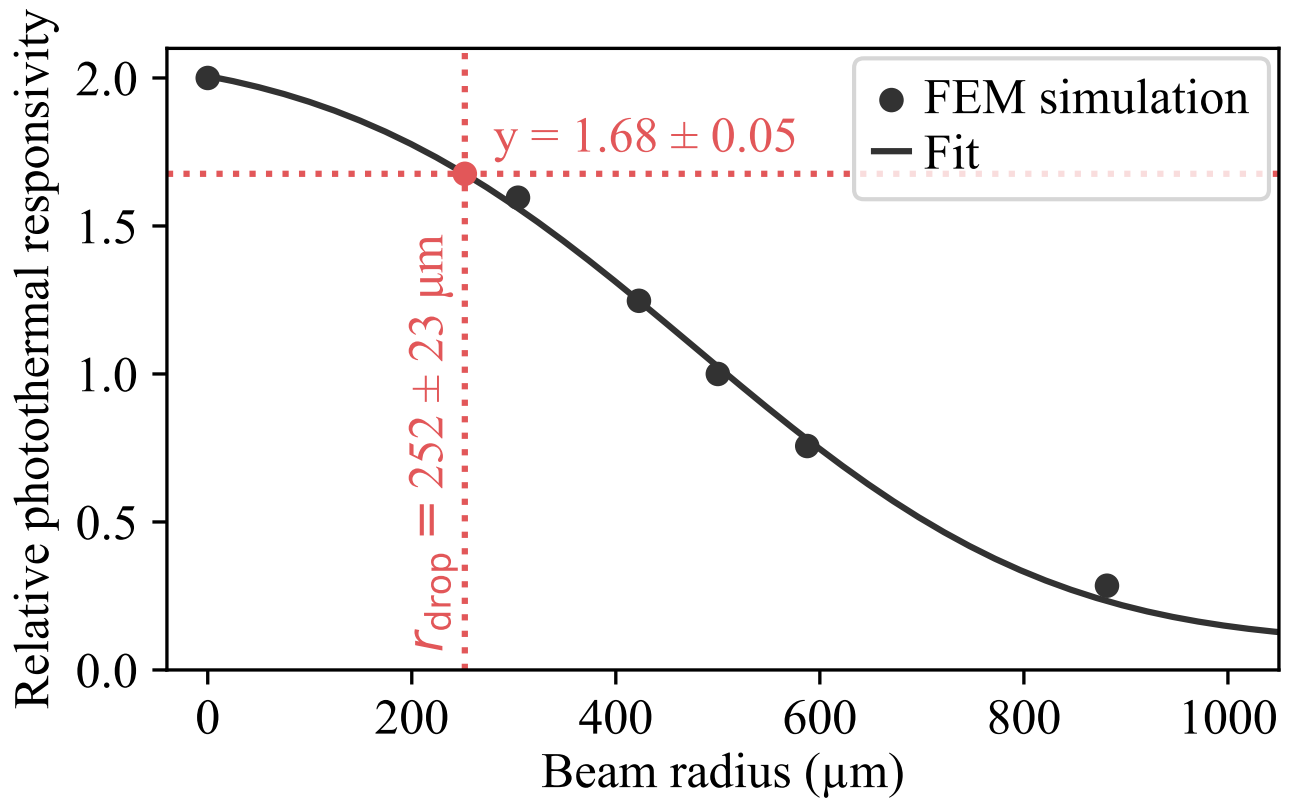


Fig. S8. Dependence of relative photothermal responsivity on the IR beam radius. Data obtained through FEM simulations of a $1 \times 1 \text{ mm}^2$ low-stress SiN membrane. The graph highlights how varying the beam radius affects the responsivity of the NEMS membrane due to spatial heat distribution.

Table S1. Deposited and estimated mass of PS NPs. Quantitative comparison of the deposited and estimated mass values for PS nanoparticles on NEMS chips, accompanied by their respective standard deviations. Deposited masses were derived from the dispersion concentrations and droplet volume, with uncertainties propagated from sample preparation (micropipette) and deposition (nanodropper) tools. Estimated masses were calculated using Eq. (6). The main source of uncertainty in estimated mass originates from variability in the measured absorbance at 1452 cm^{-1} .

Deposited mass (ng)	SD (ng)	Estimated mass (ng)	SD (ng)
0.62	0.03	0.8	0.5
1.2	0.1	1.0	0.1
2.5	0.1	2.7	0.2
5.0	0.3	5.5	0.5
10.0	0.5	11	1
20	1	21	1
40	2	43	3